

Low frequency tail of gravitational wave spectra from hydromagnetic turbulence

Ramkishor Sharma^{1*} and Axel Brandenburg^{1,2,3,4†}

¹ *Nordita, KTH Royal Institute of Technology and Stockholm University,
Hannes Alfvéns väg 12, SE-10691 Stockholm, Sweden*

² *The Oskar Klein Centre, Department of Astronomy,
Stockholm University, AlbaNova, SE-10691 Stockholm, Sweden*

³ *McWilliams Center for Cosmology & Department of Physics,
Carnegie Mellon University, Pittsburgh, PA 15213, USA and*

⁴ *School of Natural Sciences and Medicine, Ilia State University, 3-5 Cholokashvili Avenue, 0194 Tbilisi, Georgia*

Hydrodynamic and magnetohydrodynamic (MHD) turbulence in the early Universe can drive gravitational waves (GWs) and imprint their spectrum onto that of GWs, which might still be observable today. We study the production of the GW background from freely decaying MHD turbulence for helical and nonhelical initial magnetic fields. To understand the produced GW spectra, we develop a simple model on the basis of the evolution of the magnetic stress tensor. We find that the GW spectra obtained in this model reproduce those obtained in numerical simulations if we consider the time evolution of the low frequency tail of the stress spectrum from numerical simulations. We also show that the shapes of the produced GW frequency spectra are different for helical and nonhelical cases for the same initial magnetic energy spectra. Such differences can help distinguish helical and nonhelical initial magnetic fields from a polarized background of GWs – especially when the expected circular polarization cannot be detected directly.

I. INTRODUCTION

Magnetohydrodynamic (MHD) turbulence in the early Universe can be a powerful source of gravitational waves (GWs) that could be observable as a stochastic background today [1–5]. The frequency spectrum of these waves is related to the spectrum of the underlying turbulence. Such turbulence could be induced by the various phase transitions in the early Universe [6–9] or the possible presence of primordial magnetic fields [10–16]. These GWs produced by turbulence at an epoch of the electroweak phase transition lie in the sensitivity range of the proposed Laser Interferometer Space Antenna and pulsar timing arrays for the turbulence induced around an epoch of the quantum chromodynamics (QCD) phase transition. Recently, various pulsar timing arrays [17–20] have reported evidence for the presence of a common spectrum process across analyzed pulsars in the search of the presence of an isotropic stochastic GW background. This evidence has been used to constrain the strength and correlation length of the magnetic fields generated at the QCD epoch [21–23]. However, the presence of a quadrupolar spatial correlation [24], a characteristics of a GW background, is yet to be claimed.

Numerical simulations have confirmed that there is indeed a direct connection between the slopes of the turbulence and GW spectra [25], except that at low frequencies, below the peak of the spectrum, the GW spectrum was found to be shallower in the simulations than what was previously expected from analytical calculations. However, there is the worry that this shallow tail could be caused by unknown numerical artifacts such as

the finite size of the computational domain and the way the turbulence is initiated in the simulations.

To address the problem of a limited computational domain, it is important to inspect the detailed temporal dynamics of the different spatial Fourier modes of the stress. In an alternative approach, the authors of Ref. [23] have recently compared numerical simulations with an analytic model, where the stress is constant for a certain interval of time that is related to the eddy turnover time corresponding to the peak wavenumber at the initial time. Their model predicts a flat spectrum whose extent depends on the duration over which the stress is held constant. In this way, it was possible to determine an effective duration for a given numerical simulation. Their model is therefore descriptive rather than predictive.

In another recent approach, the authors of Ref. [26] have focused on the importance of unequal time correlation functions of the Fourier components of the velocity field for purely hydrodynamic turbulence. While the authors acknowledge the potential importance of the initial growth phase of the turbulence, they also show that there is no inverse cascade in their simulations. This is different from MHD turbulence, which can display inverse cascading even in the absence of net magnetic helicity. This will be crucial to the approach discussed in the present paper.

In the simulations of Ref. [23], the wavenumber corresponding to the peak of the GW spectrum and the wavenumbers below that corresponding to the horizon size at the initial time are well resolved. Since the stress appears explicitly in the linearized GW equation, we also provide the evolution of the stress spectrum for these simulations. Second, we develop a simple model, motivated by the stress evolution seen in simulations, to explain the GW spectrum obtained in simulations. In this model, our main focus is to understand the nature of the GW spec-

* ramkishor.sharma@su.se

† brandenb@nordita.org

trum below the wavenumber corresponding to the peak of the spectrum. We call this part the low frequency tail of the GW spectrum. We emphasize that the Hubble horizon wavenumber poses an ultimate cutoff for the flat spectrum toward low wavenumbers.

This paper is organized as follows. In Section II, we discuss the evolution of the magnetic field, stress, and GW spectrum in our new runs. In this section, we also discuss how the stress spectrum evolves when inverse transfer and inverse cascade turbulence regimes correspond to the evolution of the nonhelical and helical magnetic fields in the early Universe. In Section III, we discuss the model to explain the low frequency tail of the GW spectrum. Further, in Section IV, we compare the GW spectrum obtained from our numerical simulations and our model. We conclude in Section V.

II. NONHELICAL AND HELICAL CASCADES

Various phenomena such as primordial magnetic fields and phase transitions can lead to the generation of turbulence in the early Universe. The stress associated with magnetic fields and turbulence lead to the production of GWs. This has been studied in the literature both analytically [4, 27–29] and numerically [23, 25, 26, 30, 31]. In the present paper, we perform new simulations of decaying MHD turbulence, where we resolve the scales which are smaller than the Hubble horizon size at the initial time. Before explaining the simulations in detail, let us begin by summarizing the basic equations.

A. GWs from MHD turbulence

We follow here the formalism of Ref. [25, 32], where conformal time is normalized to unity at the initial time. One could associate this with the electroweak phase transition, for example. The velocity \mathbf{u} is normalized to the speed of light. The magnetic field $\mathbf{B} = \nabla \times \mathbf{A}$ is written in terms of the magnetic vector potential \mathbf{A} , and the current density is written as $\mathbf{J} = \nabla \times \mathbf{B}$. Following Ref. [33], the energy density ρ includes the restmass density, so its evolution equation obeys a continuity equation that also includes magnetic energy terms. As in [32], ρ is normalized to the critical energy density for a flat Universe. We solve for the Fourier transformed plus and cross polarizations of the gravitational strain, \tilde{h}_+ and \tilde{h}_\times , which are driven by the corresponding projections of the stress, which, in turn, is composed of kinetic and magnetic contributions,

$$\mathsf{T}_{ij} = \frac{4}{3}\gamma_{\text{Lor}}^2 \rho u_i u_j - B_i B_j + \dots, \quad (1)$$

where $\gamma_{\text{Lor}} = (1 - \mathbf{u}^2)^{-1/2}$ is the Lorentz factor, and the ellipsis denotes terms proportional to δ_{ij} , which do not contribute to the projected source $\tilde{T}_{+/\times}$.

Assuming the Universe to be conformally flat, its expansion can be scaled out by working with conformal time t and comoving variables [33]. We use the fact that in the radiation-dominated era, the scale factor grows linearly with conformal time. The only explicit occurrence of conformal time is then in the GW equation, where a $6/t$ factor occurs in the source term [32]. The full set of equations is therefore

$$\frac{\partial \mathbf{B}}{\partial t} = \nabla \times [\mathbf{u} \times \mathbf{B} + \nabla \times \mathbf{B}], \quad (2)$$

$$\frac{D\mathbf{u}}{Dt} = \frac{1}{\rho} \nabla \cdot (2\rho\nu\mathbf{S}) - \frac{1}{4} \nabla \ln \rho + \frac{\mathbf{u}}{3} (\nabla \cdot \mathbf{u} + \mathbf{u} \cdot \nabla \ln \rho) - \frac{\mathbf{u}}{\rho} [\mathbf{u} \cdot (\mathbf{J} \times \mathbf{B}) + \eta \mathbf{J}^2] + \frac{3}{4\rho} \mathbf{J} \times \mathbf{B}, \quad (3)$$

$$\frac{\partial \ln \rho}{\partial t} = -\frac{4}{3} (\nabla \cdot \mathbf{u} + \mathbf{u} \cdot \nabla \ln \rho) + \frac{1}{\rho} [\mathbf{u} \cdot (\mathbf{J} \times \mathbf{B}) + \eta \mathbf{J}^2],$$

$$\frac{\partial^2}{\partial t^2} \tilde{h}_{+/\times}(\mathbf{k}, t) + k^2 \tilde{h}_{+/\times}(\mathbf{k}, t) = \frac{6}{t} \tilde{T}_{+/\times}(\mathbf{k}, t), \quad (4)$$

where $D/Dt \equiv \partial/\partial t + \mathbf{u} \cdot \nabla$ is the advective derivative, η is the magnetic diffusivity, ν is the kinematic viscosity, $\mathsf{S}_{ij} = \frac{1}{2}(u_{i,j} + u_{j,i}) - \frac{1}{3}\delta_{ij}\nabla \cdot \mathbf{u}$ are the components of the rate-of-strain tensor \mathbf{S} with commas denoting partial derivatives. Fourier transformation in space is denoted by a tilde. In all cases studied in this paper, the initial conditions are such that \mathbf{B} consists of a weak Gaussian-distributed seed magnetic field, $\mathbf{u} = 0$, $\rho = 1$.

We work with spectra that are defined as integrals over concentric shells in wavenumber space \mathbf{k} with $k = |\mathbf{k}|$. They are normalized such that their integrals over k give the mean square of the corresponding quantity, i.e., $\int \text{Sp}(\mathbf{B}) dk = \langle \mathbf{B}^2 \rangle$, where $\text{Sp}(\mathbf{B}) = \text{Sp}(B_x) + \text{Sp}(B_y) + \text{Sp}(B_z)$. Likewise, $\text{Sp}(\mathbf{h}) = \text{Sp}(h_+) + \text{Sp}(h_\times)$ is defined as the sum over the two polarization modes. Of particular interest will also be the stress spectrum $\text{Sp}(\mathbf{T})$, which is defined analogously through $\text{Sp}(\mathbf{T}) = \text{Sp}(T_+) + \text{Sp}(T_\times)$. To study the evolution of the stress at selected Fourier modes, we compute $|T(k, t)| \equiv \sqrt{\text{Sp}(\mathbf{T})/4\pi k^2}$, which scales the same way as $|\tilde{T}_+(k, t)|$ and $|\tilde{T}_\times(k, t)|$.

B. Evolution of the stress and strain spectra

To put our results into perspective and compare with earlier work, we study cases of suddenly initiated turbulence. We perform simulations similar to those of Ref. [25] by using as initial condition for the magnetic field a random Gaussian-distributed magnetic field with a k^4 spectrum for $k < k_p$ and a $k^{-5/3}$ spectrum for $k > k_p$. For details of such a magnetic field, see Ref. [34]. As initial condition for the GW field, we assume that h and \dot{h} vanish. The strength of the GW field is then strongly determined by the sudden initialization of a fully developed turbulence spectrum. The details of the simulations is given in Table I. In this table, the first column represents the name of the runs, $\mathcal{E}_{\text{EM}}^i$ is the initial value of the magnetic energy density compared to the background

TABLE I. Summary of simulation parameters

Run	\mathcal{E}_M^i	k_p	$\mathcal{E}_{\text{GW}}^{\text{sat}}$	$\Omega_{\text{GW}}^{\text{sat}}$
hel	5.4×10^{-3}	10	3.7×10^{-7}	5.9×10^{-12}
nonhel	5.5×10^{-3}	10	3.5×10^{-7}	5.6×10^{-12}

energy density, k_p is the wavenumber at which the magnetic energy spectrum peaks and it is normalized by the wavenumber corresponding to the Hubble horizon size at the initial time, $\mathcal{E}_{\text{GW}}^{\text{sat}}$ is the value of the GW energy density after saturation compared to the background energy density, and $\Omega_{\text{GW}}^{\text{sat}}$ is the density parameter of GWs, representing the ratio of the GW energy density compared to the critical energy density at present. $\Omega_{\text{GW}}^{\text{sat}}$ has been calculated considering the production of GWs around the electroweak phase transition.

In Figures 1 and 2, we show spectra of the magnetic field, the TT-projected stress, the strain derivative, and the strain for runs with and without magnetic helicity, respectively. Inverse cascading is seen in the magnetic energy spectra, which leads to the expected increase of the spectral stress at small k ; see Figures 1(a) and (b) for the helical case. We also see in Figure 1(c) that the GW energy spectrum has a maximum at $k \sim 20$, which is not present in the nonhelical case; cf. Figure 2(c). Their spectra fall off toward smaller k proportional to k and $k^{1.5}$ in the helical and nonhelical cases, respectively.

In Figures 3 and 4, we compare stress, strain derivative, and strain spectra for helical and nonhelical runs with similar values of the initial Alfvén speed of about 0.1. In the helical case with inverse cascading, the stress increases with time at small k . By contrast, in the nonhelical case, the stress always decreases at small k . In spite of these differences, the GW spectra are not so different in the two cases. Both show a drop for $k < 1$ and a nearly flat spectrum in the interval $1 < k < 10$, which is below the peak at $2k_p = 20$. In Figures 3 and 4, we also show the evolution of the phase, $\arg(\tilde{T})$, for different k values. From these figures, it is evident that $\arg(\tilde{T})$ remains constant for some time and starts evolving more rapidly after that. It is also interesting to note that the amplitude of $|\dot{\tilde{h}}|$ increases up to the time until which $\arg(\dot{\tilde{h}})$ is roughly constant. After this time, $|\dot{\tilde{h}}|$ enters an oscillatory regime and its amplitude does not change much. This conclusion applies for both runs shown in Figures 3 and 4 and it leads us to develop a simple model to understand the GW spectrum in these cases. In this model we replace the stress, \tilde{T} by its magnitude, $|\tilde{T}|$ discussed in Section III. Further, to understand the role of the phases of the stress tensor in the production of GWs, we run two new simulations analogous to Runs hel and nonhel where we replace $\tilde{T}(k, t)$ with its modulus at each time step. The final GW spectrum in these new runs

turn out to be same as Runs hel and nonhel and these are shown in Figure 5. The comparisons of helical and nonhelical runs are shown in parts (a) and (b) of this figure, respectively. Dashed red and orange curves at times $t = 1.5$ and $t = 37$ respectively, are for the case when $\tilde{T}(\mathbf{k}, t)$ has been replaced by its modulus. It is evident from the figure that there is hardly any difference in the actual $\text{Sp}(\dot{\tilde{h}})$ and the spectra obtained after replacing the stress with its modulus. On the basis of this observation, we develop a model to obtain the GW spectrum from the time evolution of the spectrum of the stress tensor.

A striking difference between the helical and nonhelical cases is a more pronounced peak in the spectral GW energy. As we show in Appendix A, this is due to the fact that the stress spectrum for the nonhelical case is different from that of the helical case due to the presence of additional helical contributions to the two-point correlation of the magnetic field vectors. This difference is shown in Figure 6 and the details are explained in the next section.

C. Overall behavior of the stress

At the most minimalistic level, we can say that the magnetic field shows an approximately self-similar evolution at late times, where for the helical case, the peak value of $E_M(k, t)$ is unchanged, but the position of the peak k_p goes to progressively smaller values as $k_p \sim t^{-2/3}$.

To understand the consequences for the evolution of the stress, let us now consider an idealized model, where $E_M(k) \equiv \text{Sp}(\mathbf{B})/2$ has a k^4 subinertial range, where $k < k_p$, with $k_p(t)$ being the peak wavenumber, and a $k^{-5/3}$ inertial range spectrum for $k > k_p$. The spectrum of the transverse traceless part of the stress, $\text{Sp}(\mathbf{T})/2$, can be computed analytically using the expressions given in Appendix A [for details, see 35, 36] and is shown in Figures 7 and 8 for the helical and nonhelical cases, respectively. In these figures, we take three instances where the magnetic peaks are at wavenumbers $k_p = 1, 0.3$, and 0.1.

For the helical case, the position of the peak of $E_M(k)$ is unchanged. We see that, in agreement with earlier work [25], the positions of the peak of $\text{Sp}(\mathbf{T})$ are always at $2k_p$. However, even though the peak values of $E_M(k)$ are unchanged, except for the factor of two, those of $\text{Sp}(\mathbf{T})$ are not and decay. Nevertheless, at small k , $\text{Sp}(\mathbf{T})$ still increases proportional to k_p^{-1} . If $k_p \propto t^{-2/3}$, as expected for helical turbulence [37–39], we find that $\text{Sp}(\mathbf{T}) \propto t^{2/3}$ for small k .

For the nonhelical case, as shown in Ref. [39], the peak of the spectrum decreases with decreasing values of k_p proportional to k_p^β , where β is an exponent that can be between one and four. In Figure 8, we present the case with $\beta = 1$ and find that now $\text{Sp}(\mathbf{T})(k) \propto k_p$ for small k and $\propto k_p^{14/3}$ for large k . If $k_p \propto t^{-1/2}$, as expected for

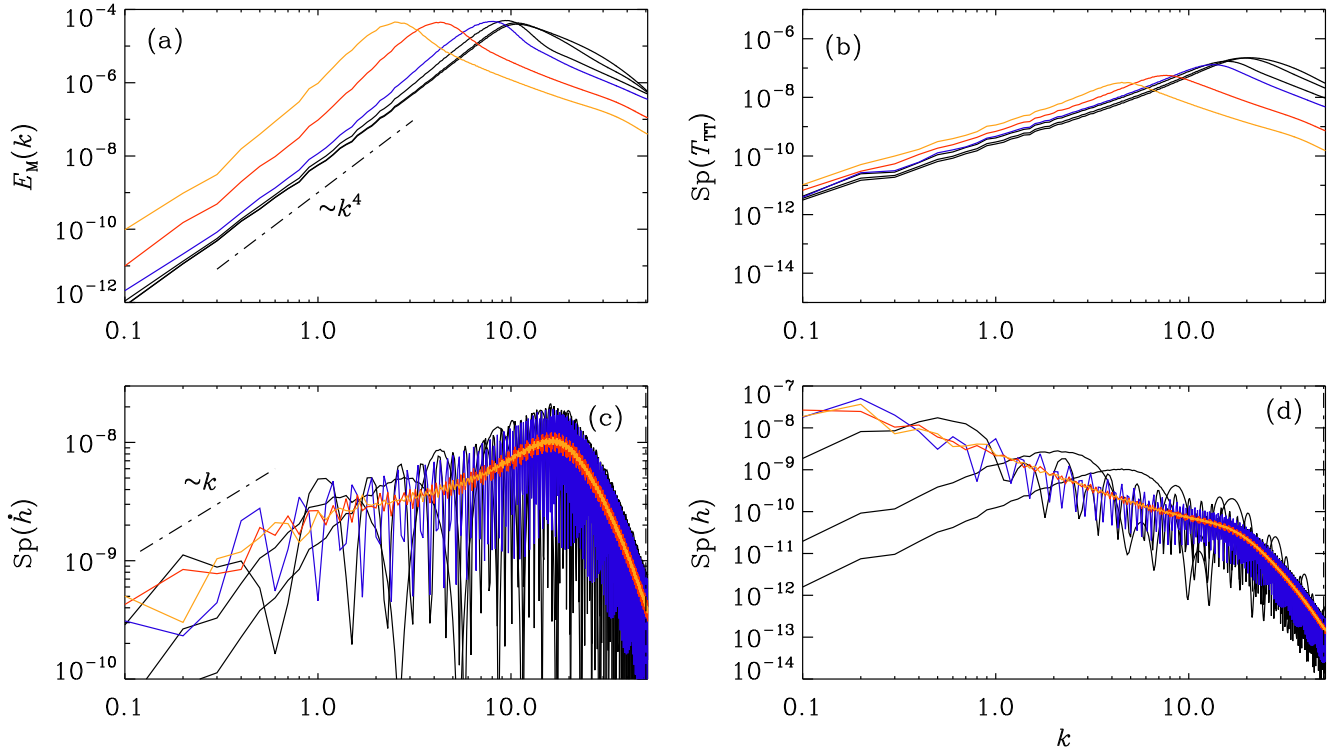


FIG. 1. Spectra of the magnetic field, the TT-projected stress, the strain derivative, and the strain for suddenly initiated turbulence with magnetic helicity.

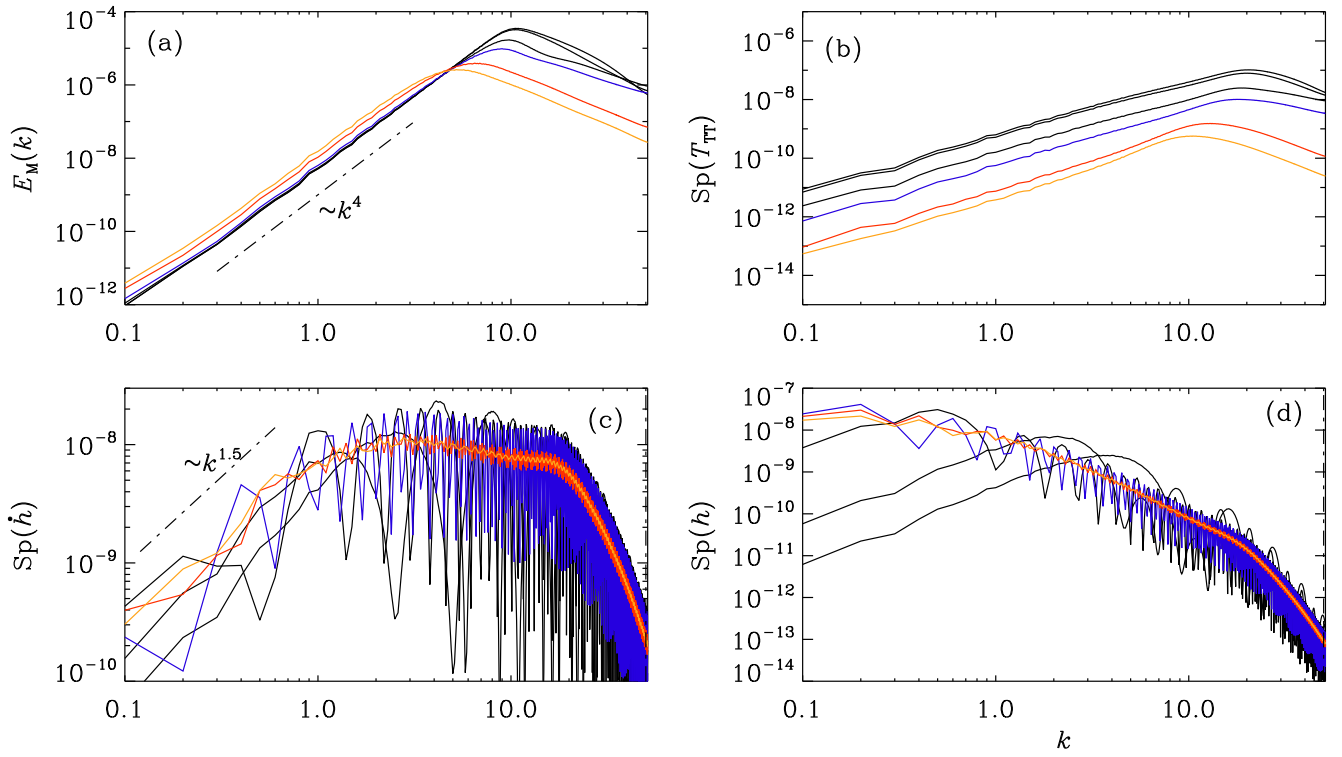


FIG. 2. Same as Figure 1, but for the nonhelical case. k_μ

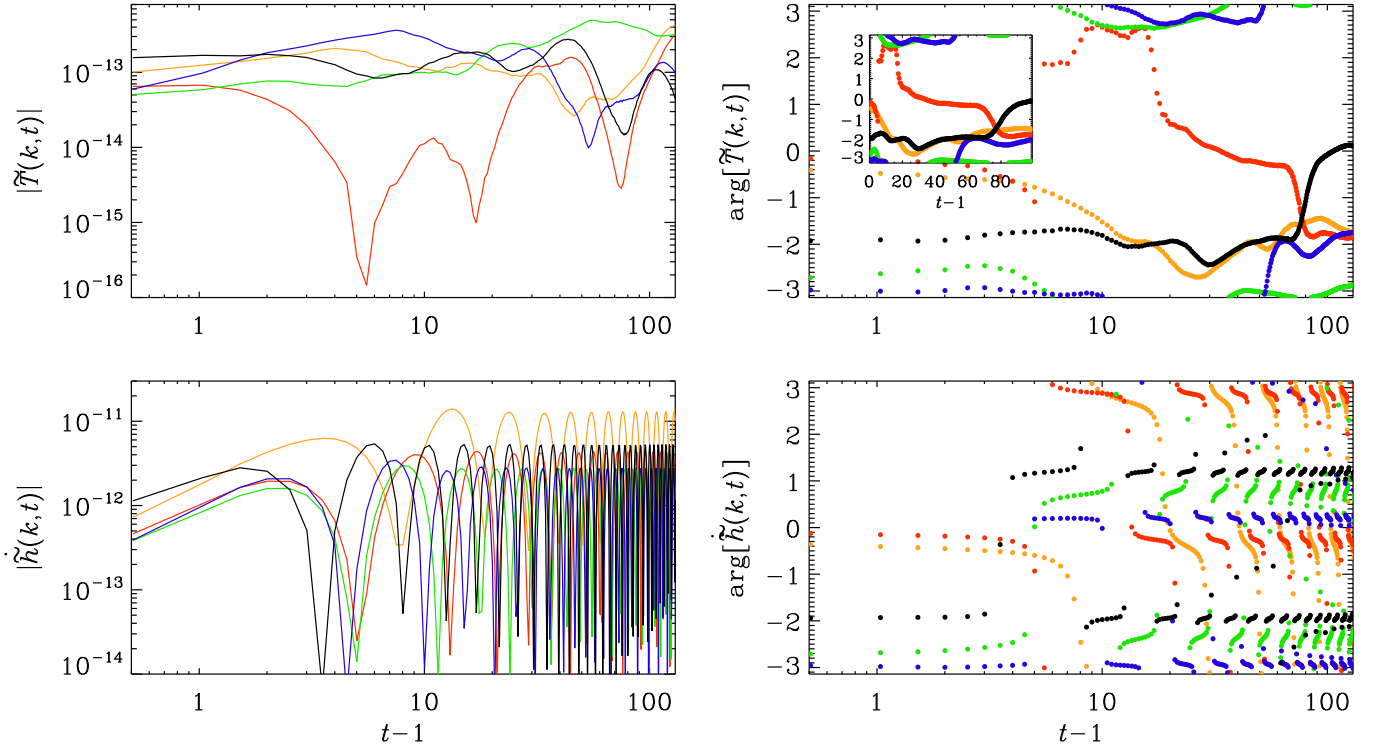


FIG. 3. Modulus and phase of $\tilde{T}(k,t)$ and $\tilde{h}(k,t)$ for the helical case for $\mathbf{k} = (k, 0, 0)$ with $k = 0.3$ (orange), 0.4 (red), 0.5 (green), 0.6 (blue), and 0.7 (black). The inset shows the phase with a linear abscissa.

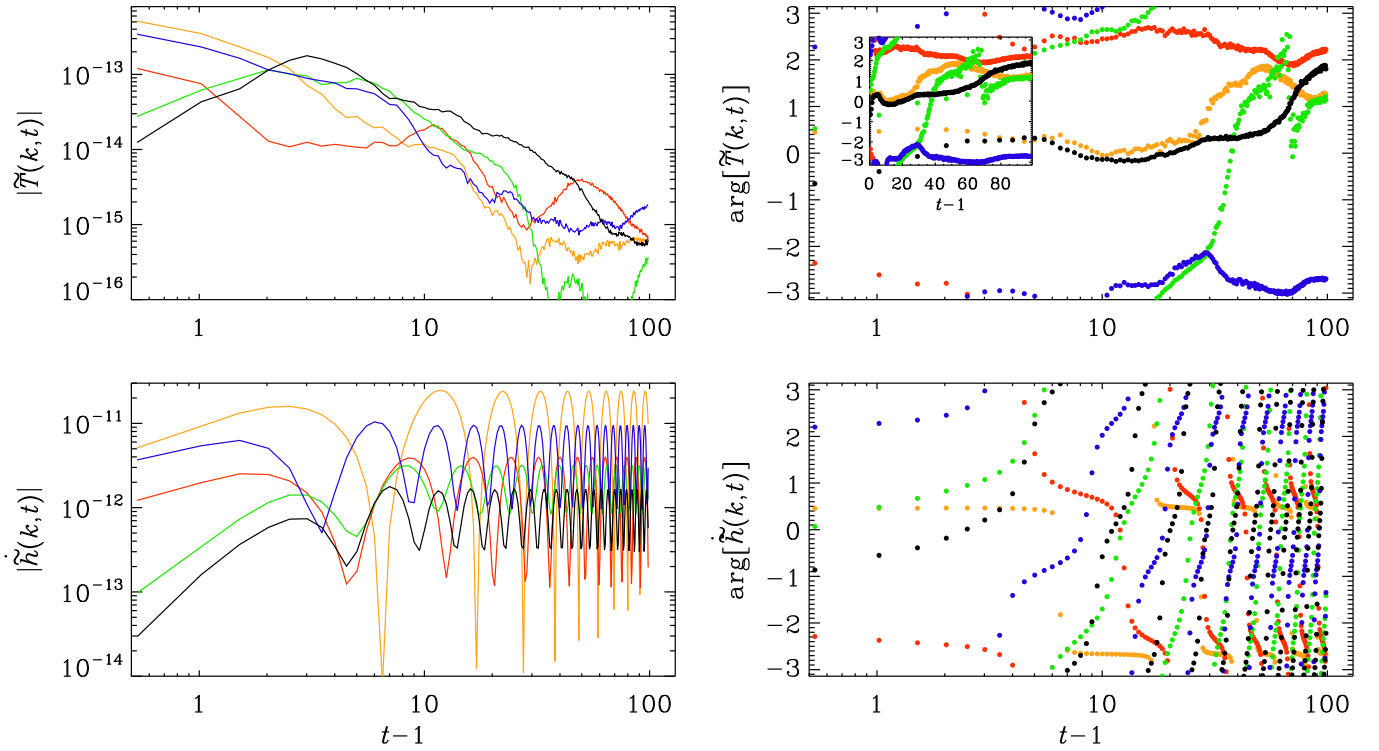


FIG. 4. Same as Figure 3, but for the nonhelical case.

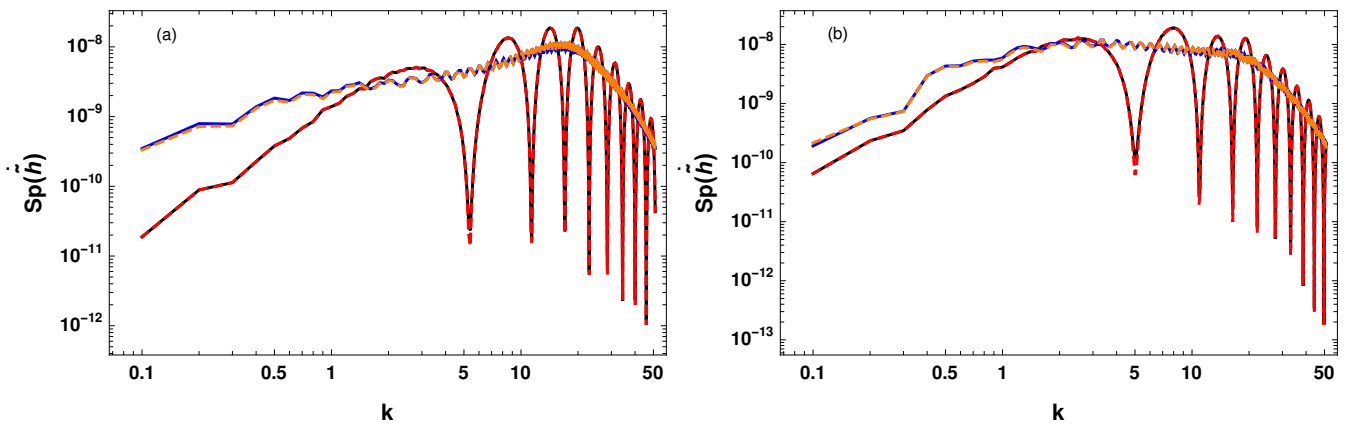


FIG. 5. $\text{Sp}(\dot{h})(k, t)$ vs k : (a) The solid black and blue curves represent $\text{Sp}(\dot{h})(k, t)$ at times $t = 1.5$ and $t = 37$ for run hel. The dashed red and orange curves show $\text{Sp}(\dot{h})(k, t)$ for the case when the stress spectrum has been replaced by its modulus in the GW evolution equation. (b) Same as (a), but for run nonhel.

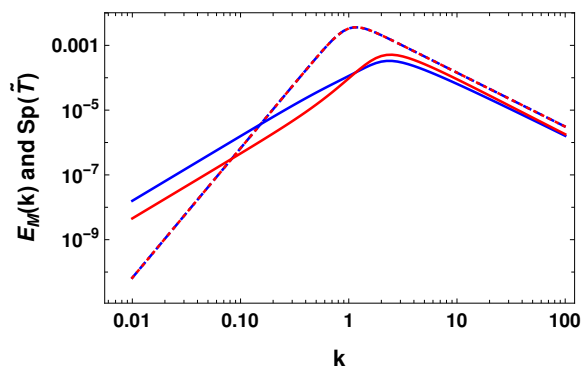


FIG. 6. In this figure, magnetic field energy spectrum, $E_M(k)$ (Dashed curves) and $\text{Sp}(\tilde{T})$ (Solid curves) for the helical and non helical case. The blue and red curves are for nonhelical and helical case respectively.

the nonhelical case for $\beta = 1$, $\text{Sp}(\tilde{T}) \propto t^{-1/2}$ for small k .

Recently, it has been found that the Saffman helicity invariant is well conserved in nonhelical magnetically dominated decaying turbulence [40], which implies $\beta = 1.5$. For the general case, we write $\text{Sp}(\tilde{T}) \propto k_p^{2\beta-1}$ (for $k < k_p$), which implies $\text{Sp}(\tilde{T}) \propto t^{-8/9}$ for $\beta = 1.5$ and $k_p \propto t^{-4/9}$.

It is also interesting to note that, for a given spectrum of magnetic field (blue and red dashed curve in Figure 6), $\text{Sp}(\mathbf{T})$ is different for the helical and nonhelical cases. The blue and red curves are for nonhelical and helical cases, respectively. In the helical case, $\text{Sp}(\mathbf{T})$ has smaller values compared to the nonhelical case at wavenumbers below k_p . However, it has large values for wavenumbers around the peak and above. Such a feature of the stress spectrum also translates to the GW spectrum and that is why we see a difference in the final GW spectrum produced from helical and nonhelical cases discussed in the

previous section.

III. PREDICTIONS FROM ALGEBRAICALLY GROWING STRESS

With the detailed information above, we are now in a position to compare with the predictions from a simple time-dependent model. In this section, we compute GW spectra by considering a simple model for the time evolution of the stress. It is assumed to increase algebraically as a power law characterized by a power law index p during the time interval from $t = 1$ to t_e .

A. The model

We model the $+$ and \times polarizations of the Fourier-transformed stress, $\tilde{T}(k, t)$, as

$$\tilde{T}(k, t) = \begin{cases} \tilde{T}_0(k) t^p, & 1 \leq t \leq t_e, \\ 0, & t > t_e, \end{cases} \quad (5)$$

where $\tilde{T}_0(k) \equiv \sqrt{\langle \tilde{T}_{ij}^{TT}(\mathbf{k}) \tilde{T}_{*ij}^{TT}(\mathbf{k}) \rangle}$ represents $|\tilde{T}(k, t)|$ at the initial time and is obtained for given energy and helicity spectra of the magnetic field; see Appendix A for details. We note that the authors of Ref. [23] have developed an analytical model for the GW spectrum on the basis of the time evolution of the stress, which they assumed constant during a certain interval – unlike our case. The authors explain the location of certain breaks in their GW spectrum as a consequence of the finite duration over which the stress is constant. This duration is an empirical input parameter. In our model, by contrast, the stress evolves as a power law with an index that is in principle known from MHD theory, although we can get even better agreement with the simulations when we

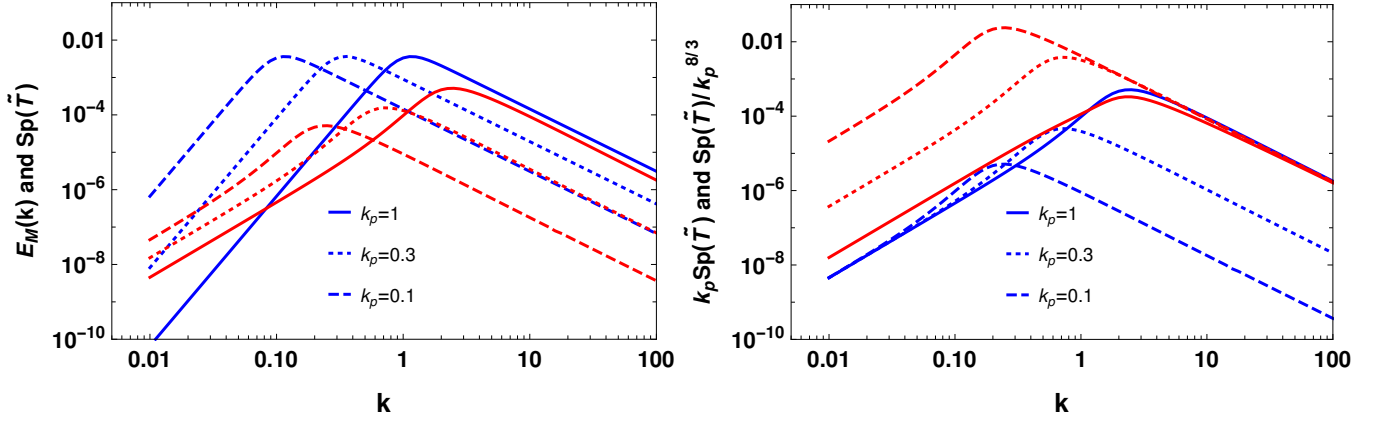


FIG. 7. Left: Solutions for $\text{Sp}(\mathbf{T}(k))$ (red) for different $E_M(k)$ (blue) for three values of k_p . Right: solutions for $\text{Sp}(\mathbf{T}(k))$ scaled by k_p (blue) and $k_p^{-8/3}$ (red), to see its scalings in the subinertial and inertial ranges, respectively.

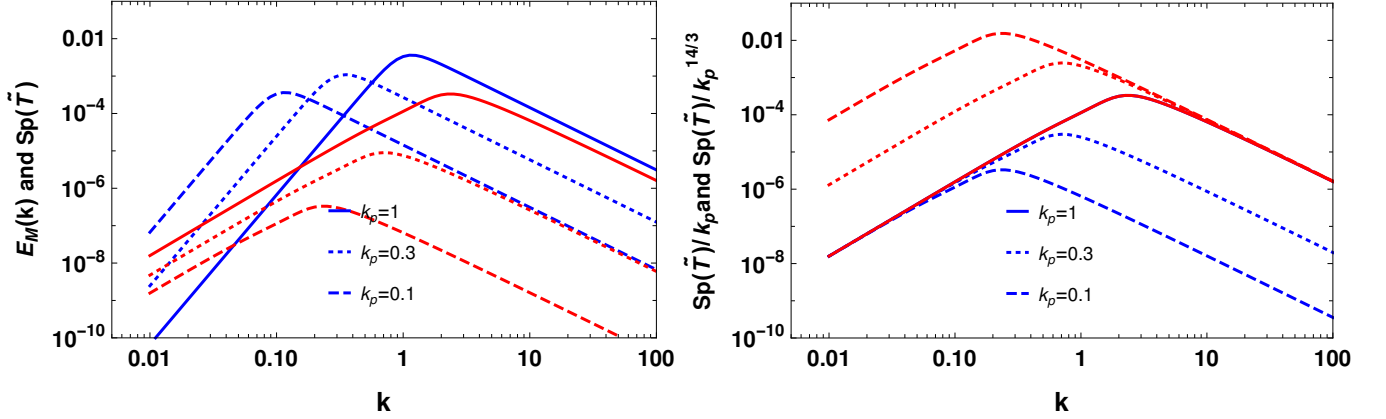


FIG. 8. Similar to Figure 7, but for a case with $\beta = 1$. On the right, the solutions for $\text{Sp}(\mathbf{T}(k))$ are scaled by k_p (blue) and $k_p^{14/3}$ (red), to see its scalings in the subinertial and inertial ranges, respectively.

take the actual power-law index that is realized in the simulations.

To obtain the GW spectrum for our model, we first solve Equation (4) for a case when the source is active during the interval $1 < t < t_e$ and thus obtain $\tilde{h}(k, t)$ and $\dot{\tilde{h}}(k, t)$. The solution for $t \geq t_e$ is given by

$$\tilde{h}(k, t) = \int_1^t \frac{\sin k(t-t')}{k} \frac{6\tilde{T}(k, t')}{t'} dt', \quad (6)$$

$$\dot{\tilde{h}}(k, t) = \int_1^t \cos k(t-t') \frac{6\tilde{T}(k, t')}{t'} dt'. \quad (7)$$

Using Equation (7) and our model for $\tilde{T}(k, t)$, we obtain

$$\dot{\tilde{h}}(k, t) = \frac{-3\tilde{T}_0(k)}{(kt_0)^p} \left\{ e^{i(kt-p\pi/2)} [\Gamma(p, ikt_e) - \Gamma(p, ikt_0)] + e^{-i(kt-p\pi/2)} [\Gamma(p, -ikt_e) - \Gamma(p, -ikt_0)] \right\}. \quad (8)$$

In the above expression, $t_0 = 1$ represents the initial time. In Figure 9(a), we show $\text{Sp}(\dot{\tilde{h}})$ at different times

for this model with $p = -1/4$. The red, blue, and black curves represent $\text{Sp}(\dot{\tilde{h}})$ at $t = 2, 4,$ and 10 , respectively. It is evident from this figure that $\text{Sp}(\dot{\tilde{h}})$ is almost flat for $1 \lesssim k \lesssim 2k_p$ and declines as $\propto k^{-11/3}$ for $k > 2k_p$. $\text{Sp}(\dot{\tilde{h}})$ is proportional to k^2 for $k < k_H$, where k_H represents the wavenumber corresponding to the Hubble horizon size at $t = t_e$. Further, as time increases, $\text{Sp}(\dot{\tilde{h}})$ at low wavenumbers ($k_H < k < 1$) grows and saturates, as is evident from Figure 9(b).

To understand the role of the power-law index in the algebraically growing part of the stress on $\text{Sp}(\dot{\tilde{h}})$, we calculate $\text{Sp}(\dot{\tilde{h}})$ for different values of p . Those are shown in the right-hand panel of Figure 10. Here, $\text{Sp}(\dot{\tilde{h}})$ is rapidly oscillating, so we plot in this figure only its envelope. From this figure, we conclude that $\text{Sp}(\dot{\tilde{h}})$ can be divided into three regime. We begin discussing first the high wavenumber regime ($k > k_0$, regime I), where k_0 represents the wavenumber corresponding to the Hubble

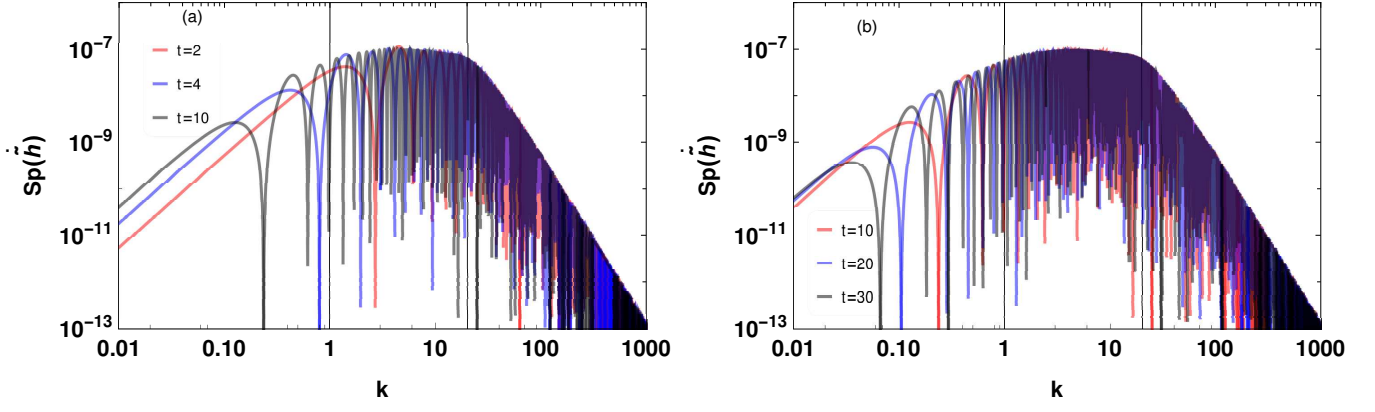


FIG. 9. (a) $\text{Sp}(\dot{\tilde{h}}(k, t))$ at different times. Here, we assume $t = t_e$, $E_M = c(k/k_p)^4 / (1 + (k/k_p)^{17/3})$, where $k_p = 10$ and $c = 10^{-4}$ and $p = -1/4$. The red, blue, and black curves are for $t_e = 2, 4,$ and 10 respectively. The two black vertical lines correspond to k_* and $2k_p$. (b) $\text{Sp}(\dot{\tilde{h}})$ at times $t_e = 10, 20,$ and 30 .

horizon at the initial time. $\text{Sp}(\dot{\tilde{h}})$ is flat and changes to $k^{-11/3}$ for $k > 2k_p$. For very low wavenumbers corresponding to the superhorizon range ($k < k_H$, regime III) $\text{Sp}(\dot{\tilde{h}})$ is proportional to k^2 . In the intermediate regime ($k_H \lesssim k \lesssim (1-p)/t_0$, regime II), $\text{Sp}(\dot{\tilde{h}})$ changes from a flat spectrum to a k^2 spectrum as the wavenumber decreases. Note that, as the wavenumbers decrease, the transition from a flat spectrum to a k^2 spectrum is faster for the case when $p = -1/4$ than $p = 1/3$. The wavenumber at which this transition occurs depends on the value of p and can be understood as follows. In the algebraically growing phase, the typical time scale over which \tilde{T}/t decays, is $\delta t_T \sim t/(1-p)$ and the typical time scale for sourcing GWs at a given wavenumber k just after $t = 1$ is $\delta t_{\text{GW}} \sim 1/k$, as can be inferred from the cosine function in Equation (7). The value of \tilde{T}/t does not change much when $\delta t_{\text{GW}}/\delta t_T \leq 1$. This implies that, for $k > (1-p)/t_0$, there will be a finite interval during which \tilde{T}/t can be assumed constant. However, for $k < (1-p)/t_0$, \tilde{T}/t always changes. The wavenumber $k \sim (1-p)/t_0$ corresponds to the wavenumber where $\text{Sp}(\dot{\tilde{h}})$ starts changing from a flat spectrum.

The nature of $\text{Sp}(\dot{\tilde{h}})$ can also be understood by writing the expression of $\dot{\tilde{h}}(k, t)$, given in Equation (8), for different limits depending on the values of kt_0 and kt_e . For $t_e \gg t_0$, which is indeed the case, and $p < 1$, Equation (8) reduces to

$$\frac{\dot{\tilde{h}}(k, t)}{6\tilde{T}_0^2(k)} \approx \begin{cases} \frac{\sin k(t-t_0)}{kt_0} & \text{(I)}, \\ \frac{\Gamma[p]}{(kt_0)^p} \cos\left(kt - \frac{p\pi}{2}\right) - \frac{\cos kt}{p} & \text{(II)}, \\ \frac{\cos kt}{p} \left[\left(\frac{t_e}{t_0}\right)^p - 1\right] & \text{(III)}. \end{cases} \quad (9)$$

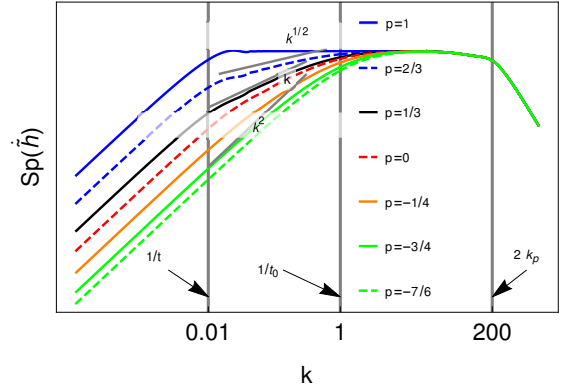


FIG. 10. $\text{Sp}(\dot{\tilde{h}})$ for different values of p . Here, the left, middle, and right black vertical lines represent the wavenumbers corresponding to the horizon size at the final time t , the initial time $t_0 = 1$, and $2k_p$, respectively.

Using this, we calculate the spectrum of $\dot{\tilde{h}}$; it is given by

$$\frac{\text{Sp}(\dot{\tilde{h}}(k, t))}{36\tilde{T}_0^2(k)} \approx \begin{cases} \left[\frac{\sin k(t-t_0)}{t_0}\right]^2 & \text{(I)}, \\ k^2 \left[-\frac{\cos kt}{p} + \frac{\Gamma[p]}{(kt_0)^p} \cos\left(kt - \frac{p\pi}{2}\right)\right]^2 & \text{(II)}, \\ k^2 \left\{\frac{\cos kt}{p} \left[\left(\frac{t_e}{t_0}\right)^p - 1\right]\right\}^2 & \text{(III)}. \end{cases} \quad (10)$$

From the above expression, we conclude that the break points for the different slopes of $\text{Sp}(\dot{\tilde{h}})$ is decided by $\tilde{T}_0^2(k)$ for $k > t_0^{-1}$. Here, $\tilde{T}_0^2(k)$ is flat for $k < 2k_p$ and proportional to $k^{-11/3}$ for $k > 2k_p$. For the superhorizon modes, i.e., $k < 1/t_e$, $\text{Sp}(\dot{\tilde{h}})$ is proportional to k^2 , and for wavenumbers $t_0^{-1} < k < t_e^{-1}$, $\text{Sp}(\dot{\tilde{h}})$ changes from a flat spectrum to k^2 , as shown as the blue curves in Figure 10.

In this model, we take the same algebraic evolution with a constant power-law index for all wavenumbers. In general, however, the time evolution of $\tilde{T}(k, t)$ is dif-

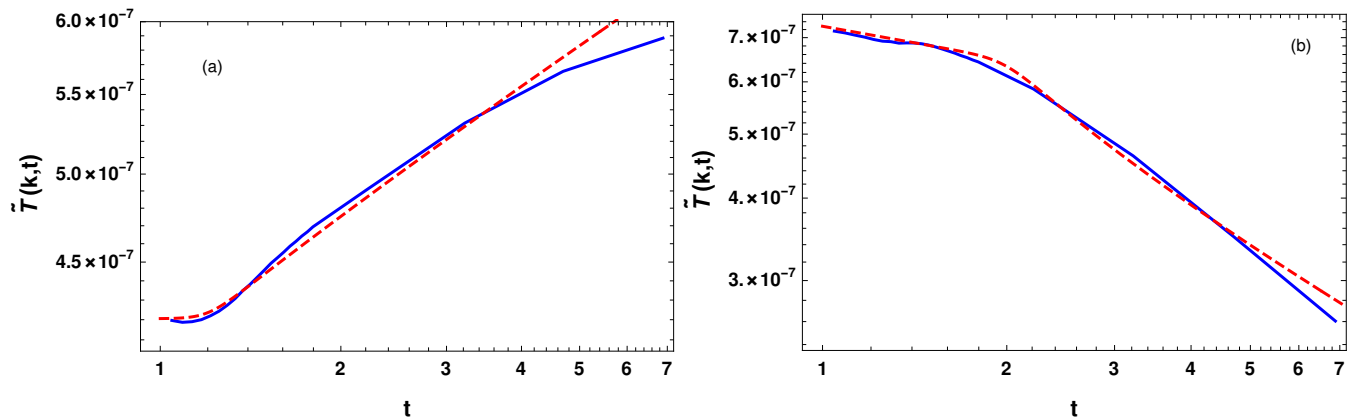


FIG. 11. $\tilde{T}(k,t)$ vs. t . (a) The blue curve corresponds to the time evolution of $\tilde{T}(k,t)$ vs t obtained from the simulation for $k = 3$ for the helical case and the red curve corresponds to a broken power law fit to the blue curve. (b) Same as (a), but for nonhelical case.

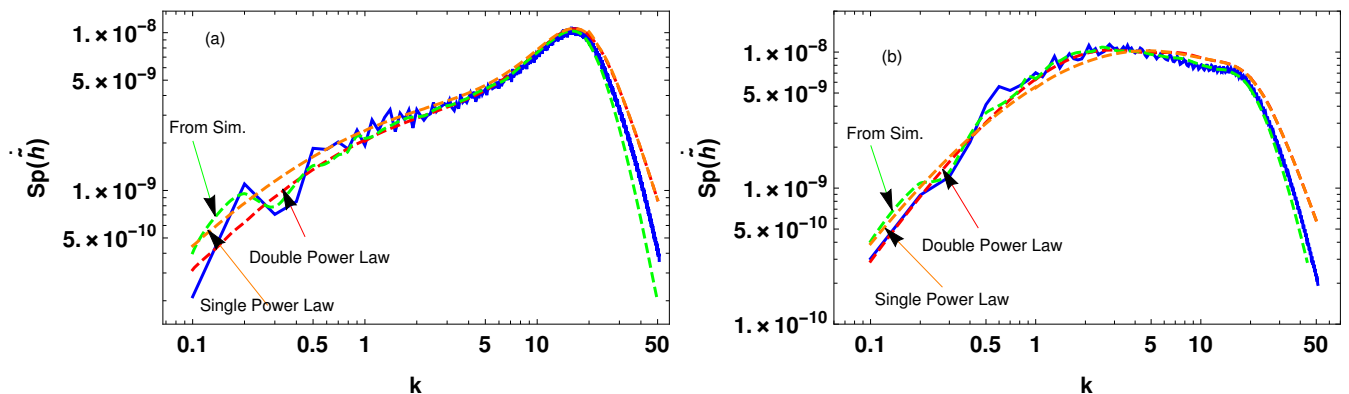


FIG. 12. $\text{Sp}(\dot{h})$ vs k : (a) The blue curve represents $\text{Sp}(\dot{h})$ corresponding to the run shown in Figure 1, respectively. The red and green curves represent the spectra obtained in the model for the time evolution of $\tilde{T}(k,t)$ given in column 2 of Table II. The orange curves represent $\text{Sp}(\dot{h})$ for the values of p given in column 1 of Table II. The red curves are for the case when $|\tilde{T}_0(k)|$ is obtained using Equation (A3) of Appendix A. For the green curves, $|\tilde{T}_0(k)|$ is taken from the simulation. (b) Same as (a), but for nonhelical case.

ferent for wavenumbers below and above the peak of $\text{Sp}(\tilde{T})(k,t)$. For the case of helical magnetic fields discussed in Figure 7, the value of $\text{Sp}(\tilde{T})$ for a particular $k < 2k_p$ at the initial time, grows as $t^{2/3}$ until the time for which $\text{Sp}(\tilde{T})$ peaks at this particular wavenumber. After this time, the value of $\text{Sp}(\tilde{T})$ for this particular k starts decreasing as $t^{-16/9}$. This implies that we would have assumed $\tilde{T}(k) \propto t^{1/3}$ for $k < k_p$ and $\tilde{T}(k) \propto t^{-8/9}$ for $k > k_p$. For the nonhelical magnetic field shown in Figure 8, $\text{Sp}(\tilde{T})$ is always decreasing. For $k < 2k_p$ at the initial time, it first decreases as $t^{-1/2}$ and later switches to $t^{-7/3}$. We study $\text{Sp}(\dot{h})$ by incorporating this and find that there is no difference in the final $\text{Sp}(\dot{h})$ compared to the one obtained in our model. This is why we did not consider the aforementioned evolution of the stress to keep the model simple.

IV. COMPARISON OF THE ANALYTICAL MODEL WITH SIMULATION RESULTS

In the above section, we discussed $\text{Sp}(\dot{h})$ in a model inspired by the fact that the GW spectrum does not change if we change the stress tensor by its modulus for decaying MHD turbulence in the early Universe. In this model, we approximate the stress tensor by $|T(k,t)| \equiv \sqrt{\text{Sp}(\mathbf{T})/4\pi k^2}$ and its time evolution is parameterized as a power law with index p ; see Figure 11. In this section, we provide a comparison for $\text{Sp}(\dot{h})$ obtained in this model with the simulation results discussed in Section II B. To compare, we show $\text{Sp}(\dot{h})$ obtained from the model and different simulations together. In Figures 12(a) and (b), we plot the spectra for the runs shown in Figures 1 and 2 and discussed in Section II B. For the dashed orange curve, \tilde{T}_0 is obtained by using Equation (A6) of Ap-

TABLE II. Time dependence of $\tilde{T}(k, t)$ taken in our analysis

Run	from MHD theory	from MHD simulations
	p	p
hel	$\left(\frac{t}{t_0}\right)^{1/3}$	$\frac{1}{(1+(t-0.2)^n)^{5/24n}}$
nonhel	$\left(\frac{t}{t_0}\right)^{-1/4}$	$\frac{t^{-1/6}}{(1+(t-1)^n)^{5/14n}}$

pendix A, where we take $E_M = c(k/k_p)^4/(1+(k/k_p)^{17/3})$ and the value of the constant c is determined such that the obtained stress spectrum matches with that of the simulation at $t = 1$. For this case, the stress spectrum evolution is modeled as a single power law and the value of p is $1/3$ and $-1/4$ for the helical and nonhelical cases, respectively. The value of p is decided from the time evolution of the low wavenumber tail of $\text{Sp}(\tilde{T})$, as discussed in Section II C. From this figure, it is concluded that the spectral nature of $\text{Sp}(\dot{\tilde{h}})$ matches well with the prediction from the model. However, there is a difference at small wavenumbers, especially for the nonhelical case. This is due to the fact that the modelling of $\text{Sp}(\tilde{T})$ by a single power does not provide a better fit to the evolution obtained in the simulation for the nonhelical case. A double power law of the form $t^{-1/3}/(1+(t-1)^n)^{5/7n}$, where n regulates the transition, here with $n = 10$, provides a better fit to $\text{Sp}(\tilde{T})$ for the low frequency tail for the nonhelical case; see Figure 11. In this figure, we plot $\tilde{T}(k, t)$ obtained from the simulation in blue color for the wavenumber $k = 3$ and the double power law fit to this curve is in red color. The double power law, which fits the $\tilde{T}(k, t)$ for the helical case, is $1/(1+(t-0.2)^n)^{5/24n}$, where $n = 20$. After considering such a time evolution, the obtained $\text{Sp}(\dot{\tilde{h}})$ is shown as the dashed red curve in Figure 12(b). For the dashed green curve, we consider $\tilde{T}_0(k) = \sqrt{\text{Sp}(\mathbf{T})}/4\pi k^2$ and $\text{Sp}(\mathbf{T})$ is obtained from the simulation at $t = 1$. These different forms of the time evolution of $\tilde{T}(k, t)$ are tabulated in Table II.

We notice that the nature of the GW spectra in the helical case are different than in the nonhelical case. There is a large power in the helical case compared to the nonhelical case around the peak of the GW spectrum for the same strength of the initial magnetic field. This is due to the presence of an additional term due to the helicity spectrum in the stress spectrum.

V. CONCLUSIONS

In this work, we have suggested a simple model to understand the GW spectrum obtained for decaying MHD turbulence in the early Universe. The Fourier-transformed stress is taken to be $|\tilde{T}(k, t)|$, i.e., we ignore changes in the phase, and its time evolution is parameter-

ized by a power law. Such a time evolution of the stress is motivated by the simulations for the decaying MHD turbulence at low wavenumbers discussed in Section II B. We find that the spectral nature of the GW spectrum is well represented by this simple model. In this work, we also show that the nature of the GW spectra in the helical case are different from those in the nonhelical case. Apart from the polarization of GW, this spectral difference may also be important in distinguishing the helical and nonhelical nature of the primordial magnetic field.

In this work, we have developed a model to understand the low frequency tail of the GW spectrum in the cases where turbulence is initiated suddenly. However, it will be more interesting to study those cases where magnetic field is generated selfconsistently, such as through the chiral magnetic effect in the early Universe [41, 42]. It would be interesting to see, if a model such as the one discussed in this paper can also explain the GW spectra obtained through the chiral magnetic effect. This, we hope to report in a future study.

ACKNOWLEDGMENTS

RS would like to thank Hongzhe Zhou for helping him analyzing the output data with the Mathematica routines of the PENCIL CODE. This work was supported by the Swedish Research Council (Vetenskapsradet, 2019-04234). Nordita is sponsored by Nordforsk. We acknowledge the allocation of computing resources provided by the Swedish National Allocations Committee at the Center for Parallel Computers at the Royal Institute of Technology in Stockholm and Linköping.

Data availability—The source code used for the simulations of this study, the PENCIL CODE, is freely available from Refs. [43]. The simulation setups and the corresponding data are freely available from Ref. [44].

Appendix A: $\text{Sp}(\tilde{T})$ in terms of magnetic field spectrum

Here, we provide the expressions for the stress spectrum in terms of the magnetic field spectrum; see Refs. [35] and [36] for details. The two-point correlation for the nonhelical magnetic field in Fourier space is given by,

$$\langle \tilde{B}_i(\mathbf{k}) \tilde{B}_j^*(\mathbf{k}') \rangle = (2\pi)^3 \delta(\mathbf{k} - \mathbf{k}') (\delta_{ij} - \hat{\mathbf{k}}_i \hat{\mathbf{k}}_j) P_{\text{SM}}(k) \quad (\text{A1})$$

Assuming a Gaussian nature of the magnetic field fluctuations, the stress spectrum is given by

$$\text{Sp}(\mathbf{T}) \equiv 4\pi k^2 \langle \tilde{T}_{ij}^{\text{TT}}(\mathbf{k}) \tilde{T}_{*ij}^{\text{TT}}(\mathbf{k}) \rangle = 4\pi k^2 \int d^3 q \left[P_{\text{SM}}(q) P_{\text{SM}}(|\mathbf{k} - \mathbf{q}|) (1 + \gamma^2 + \beta^2 + \gamma^2 \beta^2) \right]. \quad (\text{A2})$$

Here, $\tilde{T}_{ij}^{\text{T T}}(\mathbf{k}) = -B_i B_j + \frac{1}{2} \delta_{ij} B_k B_k$. In terms of the energy spectrum, $E_M(k) \equiv 4\pi k^2 P_{\text{SM}}(k)$, the above expression reduces to

$$\text{Sp}(\mathbf{T}) = \frac{1}{4\pi} \int d^3 q \frac{k^2}{q^2 |\mathbf{k} - \mathbf{q}|^2} \left[E_M(q) E_M(|\mathbf{k} - \mathbf{q}|) (1 + \gamma^2 + \beta^2 + \gamma^2 \beta^2) \right]. \quad (\text{A3})$$

In the above expressions $\gamma = \hat{\mathbf{k}} \cdot \hat{\mathbf{q}}$ and $\beta = \hat{\mathbf{k}} \cdot \widehat{\mathbf{k} - \mathbf{q}}$. For helical magnetic fields, there is an additional anti-symmetric contribution to the two-point correlation and is given by,

$$\langle \tilde{B}_i(\mathbf{k}) \tilde{B}_j^*(\mathbf{k}') \rangle = (2\pi)^3 \delta(\mathbf{k} - \mathbf{k}') \left((\delta_{ij} - \hat{\mathbf{k}}_i \hat{\mathbf{k}}_j) P_{\text{SM}}(k) + i \epsilon_{ijm} \hat{\mathbf{k}}_m P_{\text{AM}}(k) \right). \quad (\text{A4})$$

The stress spectrum for this case is given by

$$\text{Sp}(\mathbf{T}) = 4\pi k^2 \int d^3 q \left[P_{\text{SM}}(\mathbf{q}) P_{\text{SM}}(|\mathbf{k} - \mathbf{q}|) (1 + \gamma^2 + \beta^2 + \gamma^2 \beta^2) + 4\gamma\beta P_{\text{AM}}(q) P_{\text{AM}}(|\mathbf{k} - \mathbf{q}|) \right]. \quad (\text{A5})$$

In terms of the energy spectrum, $E_M(k)$, and the helicity spectrum, $H_M(k) \equiv 4\pi k^2 P_{\text{AM}}(k)$, the above expression reduces to

$$\text{Sp}(\mathbf{T}) = \frac{1}{4\pi} \int d^3 q \frac{k^2}{q^2 |\mathbf{k} - \mathbf{q}|^2} \left[E_M(\mathbf{q}) E_M(|\mathbf{k} - \mathbf{q}|) (1 + \gamma^2 + \beta^2 + \gamma^2 \beta^2) + 4\gamma\beta H_M(q) H_M(|\mathbf{k} - \mathbf{q}|) \right]. \quad (\text{A6})$$

-
- [1] Marc Kamionkowski, Arthur Kosowsky, and Michael S. Turner. Gravitational radiation from first-order phase transitions. *Phys. Rev. D*, 49(6):2837–2851, March 1994.
- [2] Craig J. Hogan. Gravitational waves from mesoscopic dynamics of the extra dimensions. *Phys. Rev. Lett.*, 85:2044–2047, Sep 2000.
- [3] Arthur Kosowsky, Andrew Mack, and Tinatin Kahnishvili. Gravitational radiation from cosmological turbulence. *Phys. Rev. D*, 66(2):024030, July 2002.
- [4] Alexander D. Dolgov, Dario Grasso, and Alberto Nicolis. Relic backgrounds of gravitational waves from cosmic turbulence. *Phys. Rev. D*, 66(10):103505, November 2002.
- [5] Chiara Caprini and Daniel G. Figueroa. Cosmological backgrounds of gravitational waves. *CQGra*, 35(16):163001, August 2018.
- [6] Edward Witten. Cosmic separation of phases. *Phys. Rev. D*, 30:272–285, Jul 1984.
- [7] C. J. Hogan. Gravitational radiation from cosmological phase transitions. *Monthly Notices of the RAS*, 218:629–636, February 1986.
- [8] Anupam Mazumdar and Graham White. Review of cosmic phase transitions: their significance and experimental signatures. *Reports on Progress in Physics*, 82(7):076901, jun 2019.
- [9] Mark Hindmarsh, Marvin Lüben, Johannes Lumma, and Martin Pauly. Phase transitions in the early universe. *SciPost Phys. Lect. Notes*, page 24, 2021.
- [10] Michael S. Turner and Lawrence M. Widrow. Inflation-produced, large-scale magnetic fields. *Phys. Rev. D*, 37(10):2743–2754, May 1988.
- [11] T. Vachaspati. Magnetic fields from cosmological phase transitions. *PhLB*, 265:258–261, August 1991.
- [12] Bharat Ratra. Cosmological “Seed” Magnetic Field from Inflation. *Astrophysical Journal, Letters*, 391:L1, May 1992.
- [13] Ruth Durrer and Andrii Neronov. Cosmological Magnetic Fields: Their Generation, Evolution and Observation. *Astron. Astrophys. Rev.*, 21:62, 2013.
- [14] Kandaswamy Subramanian. The origin, evolution and signatures of primordial magnetic fields. *RPPPh*, 79(7):076901, may 2016.
- [15] Tanmay Vachaspati. Progress on cosmological magnetic fields. *Rep. Prog. Phys.*, 2021.
- [16] Axel Brandenburg, Yutong He, and Ramkishor Sharma. Simulations of Helical Inflationary Magnetogenesis and Gravitational Waves. *Astrophys. J.*, 922(2):192, December 2021.
- [17] Zaven Arzoumanian et al. The NANOGrav 12.5 yr Data Set: Search for an Isotropic Stochastic Gravitational-wave Background. *Astrophys. J. Lett.*, 905(2):L34, 2020.
- [18] Boris Goncharov et al. On the Evidence for a Common-spectrum Process in the Search for the Nanohertz Gravitational-wave Background with the Parkes Pulsar Timing Array. *Astrophys. J. Lett.*, 917(2):L19, 2021.
- [19] S. Chen et al. Common-red-signal analysis with 24-yr high-precision timing of the European Pulsar Timing Array: inferences in the stochastic gravitational-wave background search. *Mon. Not. Roy. Astron. Soc.*, 508(4):4970–4993, 2021.
- [20] J. Antoniadis et al. The International Pulsar Timing Array second data release: Search for an isotropic gravitational wave background. *Mon. Not. Roy. Astron. Soc.*, 510(4):4873–4887, 2022.
- [21] Andrii Neronov, Alberto Roper Pol, Chiara Caprini, and Dmitri Semikoz. NANOGrav signal from magnetohydrodynamic turbulence at the QCD phase transition in the early Universe. *Phys. Rev. D*, 103(4):L041302, February 2021.
- [22] Ramkishor Sharma. Constraining models of inflationary magnetogenesis with NANOGrav data. *Phys. Rev. D*, 105(4):L041302, February 2022.
- [23] Alberto Roper Pol, Chiara Caprini, Andrii Neronov, and Dmitri Semikoz. The gravitational wave signal from primordial magnetic fields in the Pulsar Timing Array frequency band. *arXiv e-prints*, page arXiv:2201.05630, January 2022.
- [24] R. W. Hellings and G. S. Downs. Upper limits on the isotropic gravitational radiation background from pulsar

- timing analysis. *Astrophysical Journal, Letters*, 265:L39–L42, February 1983.
- [25] Alberto Roper Pol, Sayan Mandal, Axel Brandenburg, Tina Kahniashvili, and Arthur Kosowsky. Numerical simulations of gravitational waves from early-universe turbulence. *Phys. Rev. D*, 102(8):083512, October 2020.
- [26] Pierre Auclair, Chiara Caprini, Daniel Cutting, Mark Hindmarsh, Kari Rummukainen, Danièle A. Steer, and David J. Weir. Generation of gravitational waves from freely decaying turbulence. 5 2022.
- [27] Arthur Kosowsky, Andrew Mack, and Tinatin Kahniashvili. Gravitational radiation from cosmological turbulence. *PhRvD*, 66:024030, Jul 2002.
- [28] Grigol Gogoberidze, Tina Kahniashvili, and Arthur Kosowsky. Spectrum of gravitational radiation from primordial turbulence. *Phys. Rev. D*, 76(8):083002, October 2007.
- [29] Tina Kahniashvili, Arthur Kosowsky, Grigol Gogoberidze, and Yuri Maravin. Detectability of gravitational waves from phase transitions. *PhRvD*, 78:043003, Aug 2008.
- [30] Alberto Roper Pol, Sayan Mandal, Axel Brandenburg, and Tina Kahniashvili. Polarization of gravitational waves from helical MHD turbulent sources. *JCAP*, submitted, page arXiv:2107.05356, July 2021.
- [31] Tina Kahniashvili, Axel Brandenburg, Grigol Gogoberidze, Sayan Mandal, and Alberto Roper Pol. Circular polarization of gravitational waves from early-Universe helical turbulence. *PhRvR*, 3(1):013193, February 2021.
- [32] Alberto Roper Pol, Axel Brandenburg, Tina Kahniashvili, Arthur Kosowsky, and Sayan Mandal. The timestep constraint in solving the gravitational wave equations sourced by hydromagnetic turbulence. *GApFD*, 114:130–161, March 2020.
- [33] Axel Brandenburg, Kari Enqvist, and Poul Olesen. Large-scale magnetic fields from hydromagnetic turbulence in the very early universe. *Phys. Rev. D*, 54(2):1291–1300, July 1996.
- [34] Axel Brandenburg, Tina Kahniashvili, Sayan Mandal, Alberto Roper Pol, Alexander G. Tevzadze, and Tanmay Vachaspati. Evolution of hydromagnetic turbulence from the electroweak phase transition. *Phys. Rev. D*, 96:123528, December 2017.
- [35] Chiara Caprini, Ruth Durrer, and Tina Kahniashvili. Cosmic microwave background and helical magnetic fields: The tensor mode. *Phys. Rev. D*, 69(6):063006, March 2004.
- [36] Ramkishor Sharma, Kandaswamy Subramanian, and T. R. Seshadri. Gravitational wave generation in a viable scenario of inflationary magnetogenesis. *Phys. Rev. D*, 101(10):103526, May 2020.
- [37] Tadatsugu Hatori. Kolmogorov-Style Argument for the Decaying Homogeneous MHD Turbulence. *JPSJ*, 53(8):2539–, 1984.
- [38] Dieter Biskamp and Wolf-Christian Müller. Decay Laws for Three-Dimensional Magnetohydrodynamic Turbulence. *Phys. Rev. Lett.*, 83(11):2195–2198, September 1999.
- [39] A. Brandenburg and T. Kahniashvili. Classes of Hydrodynamic and Magnetohydrodynamic Turbulent Decay. *PhRvL*, 118:055102, February 2017.
- [40] David N. Hosking and Alexander A. Schekochihin. Reconnection-controlled decay of magnetohydrodynamic turbulence and the role of invariants. *Phys. Rev. X*, 11:041005, Oct 2021.
- [41] Igor Rogachevskii, Oleg Ruchayskiy, Alexey Boyarsky, Jürg Fröhlich, Nathan Kleeorin, Axel Brandenburg, and Jennifer Schober. Laminar and Turbulent Dynamos in Chiral Magnetohydrodynamics. I. Theory. *Astrophys. J.*, 846(2):153, September 2017.
- [42] Jennifer Schober, Igor Rogachevskii, Axel Brandenburg, Alexey Boyarsky, Jürg Fröhlich, Oleg Ruchayskiy, and Nathan Kleeorin. Laminar and Turbulent Dynamos in Chiral Magnetohydrodynamics. II. Simulations. *Astrophys. J.*, 858:124, May 2018.
- [43] Pencil Code Collaboration, Axel Brandenburg, Anders Johansen, Philippe Bourdin, Wolfgang Dobler, Wladimir Lyra, Matthias Rheinhardt, Sven Bingert, Nils Haugen, Antony Mee, Frederick Gent, Natalia Babkovskaia, Chao-Chin Yang, Tobias Heinemann, Boris Dintrans, Dhruvadiya Mitra, Simon Candelaresi, Jörn Warnecke, Petri Käpylä, Andreas Schreiber, Piyali Chatterjee, Maarit Käpylä, Xiang-Yu Li, Jonas Krüger, Jørgen Aarnes, Graeme Sarson, Jeffrey Oishi, Jennifer Schober, Raphaël Plasson, Christer Sandin, Ewa Karchniwy, Luiz Rodrigues, Alexander Hubbard, Gustavo Guerrero, Andrew Snodin, Illa Losada, Johannes Pekkilä, and Chengeng Qian. The Pencil Code, a modular MPI code for partial differential equations and particles: multipurpose and multiuser-maintained. *JOSS*, 6(58):2807, February 2021.
- [44] R. Sharma and A. Brandenburg. Datasets for low frequency tail of gravitational wave spectra from hydromagnetic turbulence, doi:10.5281/zenodo.6596525 (v2022.05.31). *see also* <http://norlax65.nordita.org/~brandenb/projects/LowFreqTail> for easier access.